Influence of the Mn Content on the Kinetics of Austempering Transformation in Compacted Graphite Cast Iron

J. DESIMONI, R. GREGORUTTI, K. LANERI, J.L. SARUTTI, and R.C. MERCADER

Mössbauer spectroscopy has been used to monitor the kinetics of austempering transformation in two compacted graphite (CG) cast irons alloyed with 0.11 and 0.58 wt pct of Mn, respectively. The phase relations were analyzed in terms of the Johnson–Mehl's equation, determining the kinetics parameters n (time exponent) and k (constant rate of the transformation). The values obtained were $n = 1.4$ and $k = 7.47 \times 10^{-3}\ s^{-1}$ for the low-Mn alloy, and $n = 2.2$ and $k = 3.9 \times 10^{-3}\ s^{-1}$ for the high-Mn alloy. These results, which reveal a faster kinetics for the low-Mn alloy, are coherent with metallographic observations, and the driving force obtained through the determination of the austenite carbon concentration that was determined from the Mössbauer data using the Génins model for the Fe-C configurations in the fcc lattice. The kinetics parameters are further compared to those obtained in austempered ductile iron (ADI), by analyzing the graphite morphology influence on the austempering transformation.

I. INTRODUCTION

IN the last decade, many studies[1–5] have been performed which extend to compacted graphite (CG) cast iron the austempering heat treatment widely used to improve the mechanical properties of nodular cast iron, also called austempered ductile iron (ADI). However, the dependence of the kinetics parameters on the alloy concentration remains an open question in that cast iron.

The austempering transformation in cast irons involves three stages. In *stage I*, parent austenite transforms into acicular ferrite and high-carbon austenite ($\gamma \rightarrow \alpha_{Fe} + \gamma_{hc}$), forming a microstructure called ausferrite. The mechanism of the reaction consists of the nucleation and growth of ferrite needles that reject carbon atoms into the surrounding austenite, which becomes more stable due to the increase in the carbon content, which, on its own, causes the martensitic starting point to become lower than room temperature. The fraction of austenite that has not become rich enough in carbon transforms into martensite during the cooling to room temperature. The transformation progresses until the phases reach a metastable equilibrium. At this point, the transformation stops temporarily and begins a steady-state period (*stage II*), in which the amounts of acicular ferrite and high-carbon austenite remain approximately constant. *Stage II* is also called the processing window, where optimum mechanical properties are obtained. When the metastable high-carbon austenite eventually decomposes into the more thermodynamically stable ferrite and carbides, *stage III* starts, with the consequent reduction of the mechanical properties, particularly ductility and toughness.

Mössbauer spectroscopy has been proven to be a powerful analytical technique for quantitative studies of metallurgical phenomena.[6] Because of its microscopic character, Mössbauer spectroscopy is particularly suitable to accounting for the mechanism of transformations that involve nucleation and growth processes.

Several articles have determined the kinetics of austempering transformation in cast irons, using an X-ray diffraction technique.[4,5,7–9] Mössbauer spectroscopy can be used advantageously toward this end, due to its ability to identify ferrite, austenite, martensite, and intermetallic phases. The characterization is based on the magnetic and hyperfine properties of the different phases, even for the complex phase diagram of the Fe-C system. Problems appear only when the phase under investigation contributes to the total spectrum, with a percentage below about 1 pct for materials nonenriched in ^{57}Fe. Many review articles give detailed reports of these features.[10] The case of the iron-carbon martensite is a clear example of the way in which the carbon atoms modify the hyperfine magnetic field set up by the iron neighbors, producing the appearance that several subspectra can be resolved in data with high statistics. In addition to the hyperfine-fields parameters, the different phases are distinguished by their magnetic properties. Iron phases change the magnetic regime according to the Fe-Fe distances, yielding a paramagnetic regime at room temperature for γ-iron fcc (austenite), as calculated by Fujita and Nasu.[11] Being a local probe, the Mössbauer spectroscopy atom senses the new phases formed from the very beginning of the new-phase seeds. This is an advantage with respect to the bulk or cooperative techniques and enhances its sensitivity in monitoring metallic-phase changes.

This article analyzes the kinetics of the *stage I* austempering transformation in two CG cast irons alloyed with different Mn contents and austempered at 623 K by means of the Johnson–Mehl equation.[12] The time exponent (n) related to the particular nucleation and growth conditions and the constant rate (k) associated with the nucleation and growth rate were determined in order to study Mn influence. The results are further compared to those reported in ADI,[13] to analyze the influence of graphite morphology on the austempering transformation.

J. DESIMONI and R.C. MERCADER, Professor of Departamento de Física, Facultad de Ciencias Exactas—U.N.L.P., CC. N°67 (1900) La Plata, Argentina, and Researchers of CONICET; K. LANERI, Teaching Assistant of the Facultad de Ingeniería U.N.L.P. and Fellow of ANCyT; R. GREGORUTTI, Research Assistant of LEMIT-CICPBA and Teaching Assistant of the Facultad de Ingeniería—U.N.L.P.; and J.L. SARUTTI, Research Assistant of the LEMIT-CICPBA and Professor of Facultad de Ingeniería U.N.L.P.

Manuscript submitted February 22, 1999.

Table I. Chemical Composition in Weight Percent of the Two Manganese Alloyed Compacted Graphite Cast Irons

Alloy	C	Si	Mn	Cu	P	S
A	3.40	2.35	0.58	0.04	0.01	0.02
B	3.52	2.10	0.11	0.03	0.01	0.03

Table II. Microstructural Parameters of CG Cast Iron

Alloy	N_{CG} (CG/mm^2)	L (mm)	P (mm/mm^2)
A	104	0.190	19.76
B	82	0.194	15.9

II. EXPERIMENTAL PROCEDURE

Base metal, of composition 3.6 wt pct C, 1.8 wt pct Si, 0.1 wt pct Mn, 0.05 wt pct Cu, 0.01 wt pct P, and 0.02 wt pct S, was used to produce CG cast iron in a medium-frequency induction furnace, using the sandwich technique in a ladle to treat the liquid metal. FeSiMgCeCa was added to obtain a CG morphology, and Mn and Si balances were attained by adding appropriate amounts of FeMn (C_{Mn} = 60 wt pct) and FeSi (C_{Si} = 75 wt pct). The resulting chemical composition for both cast irons is displayed in Table I.

In order to characterize the microstructure, a Reichert optical microscope, with image-analysis software (Analy SIS DOCU) for both particle count/mm^2 and measurement of the perimeter, was used. These values permit an estimation of the graphite/austenite interface (P) for both cast irons, which were calculated as the product of the average number of CG particles/mm^2 (N_{CG}) and their average perimeter (L), and the results are displayed in Table II.

Hardness tests were done with a standard Vickers hardness machine, using a load of 30 kg.

Samples 20 mm in diameter and 3-mm thick were taken from "Y-shaped" blocks (ASTM A-395) casted in sand molds. Heat treatments were performed by austenitizing at 1173 K for 30 minutes and then quenching in a salt bath held at 623 K.

The samples were specially prepared for Mössbauer spectroscopy by conventional grinding techniques to reduce their thickness down to 70 μm, using, progressively, a diamond paste of 6, 1, and 0.1 μm for the final polishing.

Mössbauer spectra were taken in transmission geometry using a ^{57}CoRh source of approximately 5 mCi and were recorded in a standard 512-channel conventional constant-acceleration spectrometer. Two sets of spectra were taken in order to analyze in detail the different phases present in the samples. One range covers velocities between −8 and +8 mm/s, and the other one covers velocities between −2 and +2 mm/s. Velocity calibration was performed against a 12-μm-thick α-Fe foil. All isomer shifts are referred to this standard at 298 K. Following Reference 14, the analysis of the spectrum for one sample was performed with a Voigt's profile for the line shape. However, the percentages obtained lay within the statistical errors of the data using Lorentzian line shapes. For this reason, all spectra were fitted to Lorentzian line shapes by a nonlinear least-squares program with constraints.

III. RESULTS AND DISCUSSION

Typical Mössbauer spectra of the higher-velocity range, corresponding to austempering times of 1, 10, and 30 minutes, are illustrated in Figure 1 for both alloys. The characteristic six lines belonging to the magnetic component, *i.e.*, the martensite and/or ferrite phases, and a central line corresponding to the nonmagnetic component, indicative of the existence of austenite, are observed. Magnetic subspectra were fitted using three different hyperfine interactions (H_1 = 33 T, δ_1 = 0.01 mm/s; H_2 = 31 T, δ_2 = 0.04 mm/s; and H_3 = 27 T, δ_3 = 0.1 mm/s), while the austenite subspectra were simulated with a quadrupole doublet and a single line, since the full complexity of the austenite Mössbauer spectra is not resolved in this velocity range. However, this does not affect the subspectra areas.

The progress of the transformation during *stage I* of austempering was analyzed by monitoring the evolution of the austenite relative fraction (f_γ) obtained (assuming an equal recoilless fraction for all phases) as a function of the austempering time. A first evidence of the Mn influence on the kinetics is observed in Figure 2, where it can be perceived that f_γ evolution is faster in the low-Mn alloy (alloy B). This result reveals a larger ferrite nucleation and growth rate which promotes a more noticeable increase of the fraction of retained austenite, which means that the time to complete stage I is shorter for alloy B. Nevertheless, at times corresponding to stage II, the mount of retained austenite is approximately similar for both alloys.

Hardness measurements also show the progress of the transformation, as can be seen in Figure 3. At early times of *stage I*, hardness values are high because martensite is the predominant structure, and, as the austempering time progresses, the hardness drops simultaneously with the advance of the ausferritic structure.

Since f_γ evolution follows a sigmoidal behavior, typical of a nucleation and growth reaction, the kinetics of transformation was analyzed using the Johnson–Mehl equation:[12,13]

$$X(t) = 1 - \exp(-kt)^n$$

where $X(t)$ is the transformed fraction, defined as

$$X(t) = (f_\gamma(t) - f_\gamma(0))/(f_\gamma(f) - f_\gamma(0))$$

where $f_\gamma(0)$ is the austenite value at time zero, while $f_\gamma(t)$ and $f_\gamma(f)$ are the relative fractions of austenite at time t and after completion of transformation, respectively.

The mechanism of the transformation is exposed by the kinetics parameters n and k. The time exponent is related to the particular nucleation and growth conditions, while the constant rate of the reaction is associated with the rate of nucleation and growth of the new phase. These kinetics parameters were determined by fitting the linearized Johnson–Mehl equation, plotted in Figure 4:

$$\log \log (1 - X(t))^{-1} = (n \log k + \log \log e) + n \log t$$

The results obtained from Figure 4 indicate that the time exponent is smaller for alloy B than for alloy A, being 1.4 and 2.2, respectively. These values imply a localized nucleation and a phase transformation controlled by an interface reaction.[15] After the nucleation sites become saturated, the advance of the transformation is further controlled by a diffusion process.[16] In the case of the austempering transformation in cast irons, there are two places where ferrite needles can nucleate: the graphite/austenite interface and the

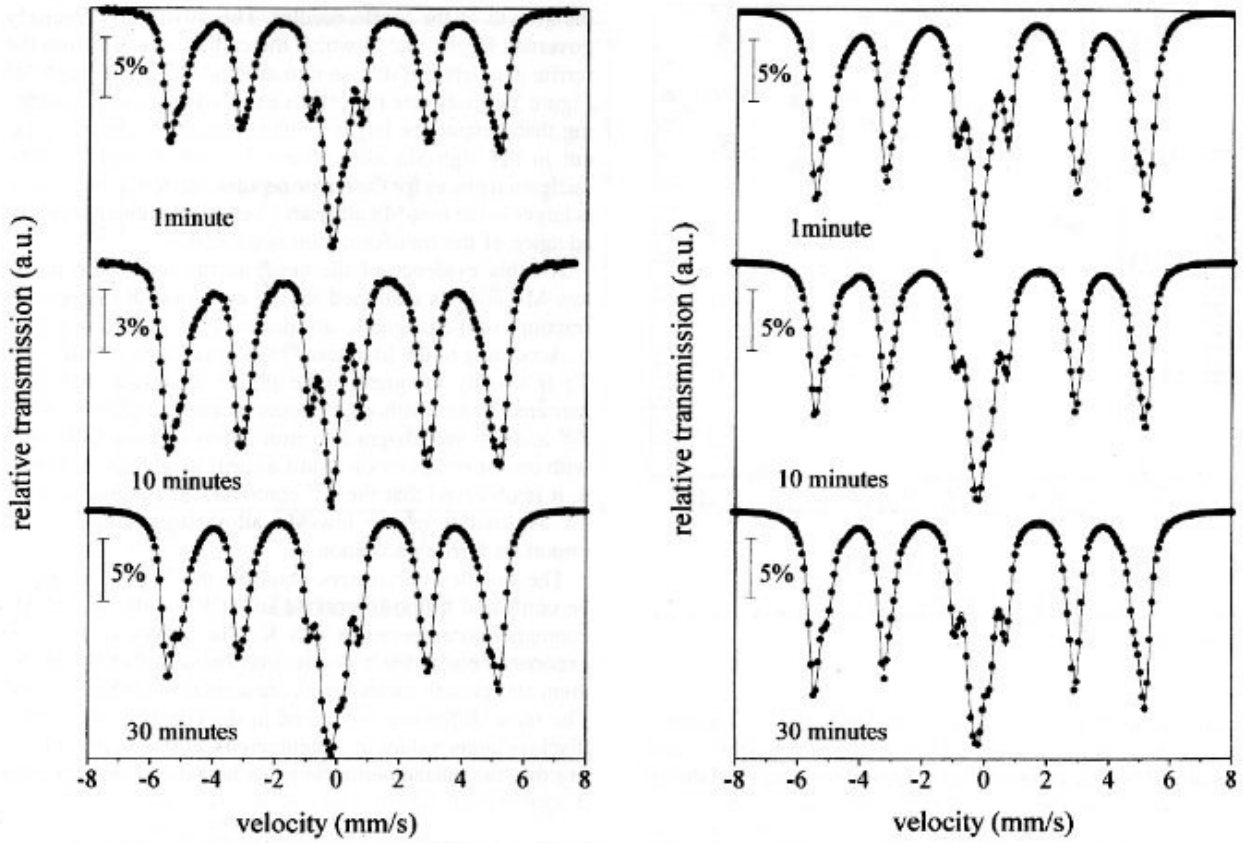

Fig. 1—Typical Mössbauer spectra belonging to alloy A (left) and alloy B (right) labeled with the austempering time.

austenite grain boundaries. This can be seen in micrographs corresponding to early times of austempering, included in Figure 5.

The Mn effects on the austempering kinetics are mainly displayed by the constant rate. The results exhibited in Figure 4 reveal that the constant rate is larger in alloy B than in

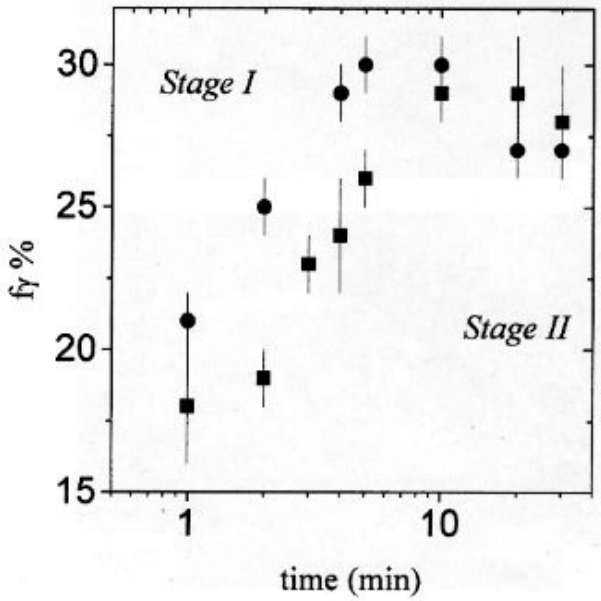

Fig. 2—Evolution of the f_γ austenite relative fraction with the austempering time: ■ alloy A, and ● alloy B.

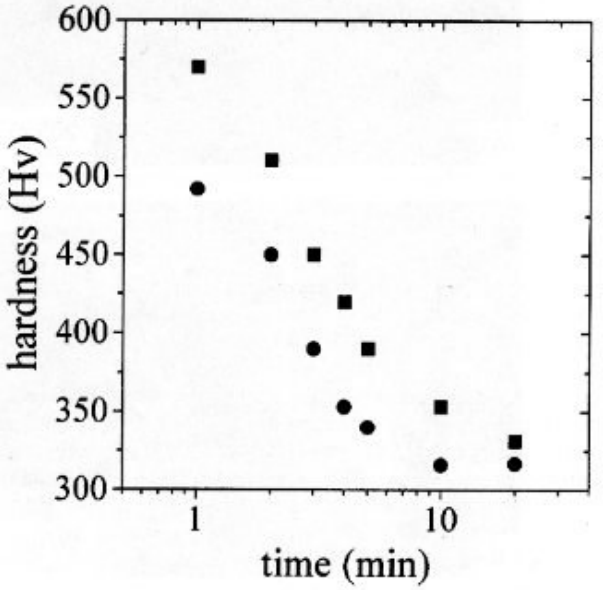

Fig. 3—Hardness evolution with the austempering time: ■ alloy A, and ● alloy B.

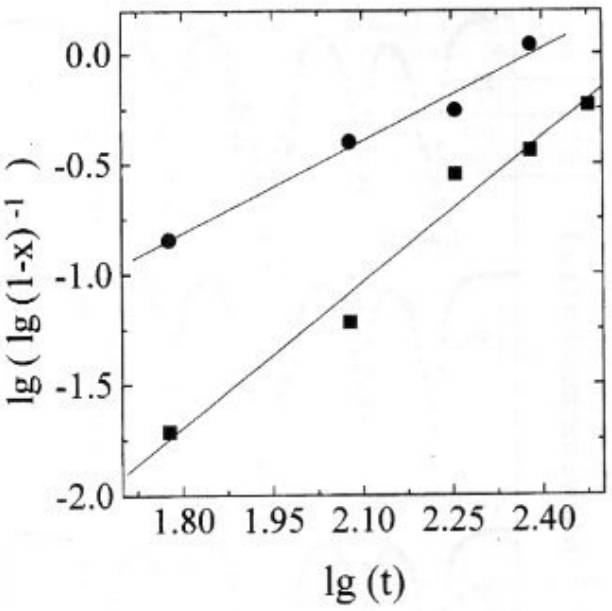

Fig. 4—Transformed linear of the Johnson–Mehl equation: ■ alloy A, and ● alloy B.

alloy A, being $7.47 \times 10^{-3}\ s^{-1}$ and $3.9 \times 10^{-3}\ s^{-1}$, respectively. Mn has the ability to delay the ferrite nucleation and to slow down the carbon diffusion into austenite,[17] retarding the growth of the ferrite needles. This advance is precisely governed by the rate at which the carbon rejected from the ferrite platelets can diffuse into austenite.[9] Micrographs of Figure 5 corroborate the results exposed previosly, illustrating that, despite the larger graphite/austenite interface present in the high-Mn alloy (Table II), which implies more nucleation places for the ferrite needles, the ferrite nucleation is larger in the low-Mn alloy and, hence, the more noticeable advance of the transformation is noticed.

Another evidence of the larger ferrite nucleation in the low-Mn alloy is exhibited by the evolution of the relative fractions of the magnetic subspectra (F_i^M), plotted in Figure 6. According to the literature,[6] the interaction F_1^M ($H = 33$ T) is usually assigned to Fe probes in ferrite and/or in martensite sites without C atoms as near neighbors, while F_2^M and F_3^M are assigned to iron atoms in martensite sites with one or more carbon atoms as near neighbors. In Figure 6, it is observed that the F_1^M contribution is higher and the F_3^M is smaller in the low-Mn alloy, suggesting a more important ferrite nucleation.

The kinetics parameters obtained in CG cast iron can be compared to those reported in ADI[13] with several Mn contents, austempered at 623 K. The values of the time exponent obtained in CG cast iron indicate that the nucleation and growth mechanisms are similar in both cast irons. The main difference is noticed in the constant rate, which displays larger values in austempered CG cast irons, indicating that the austempering kinetics is faster with respect to

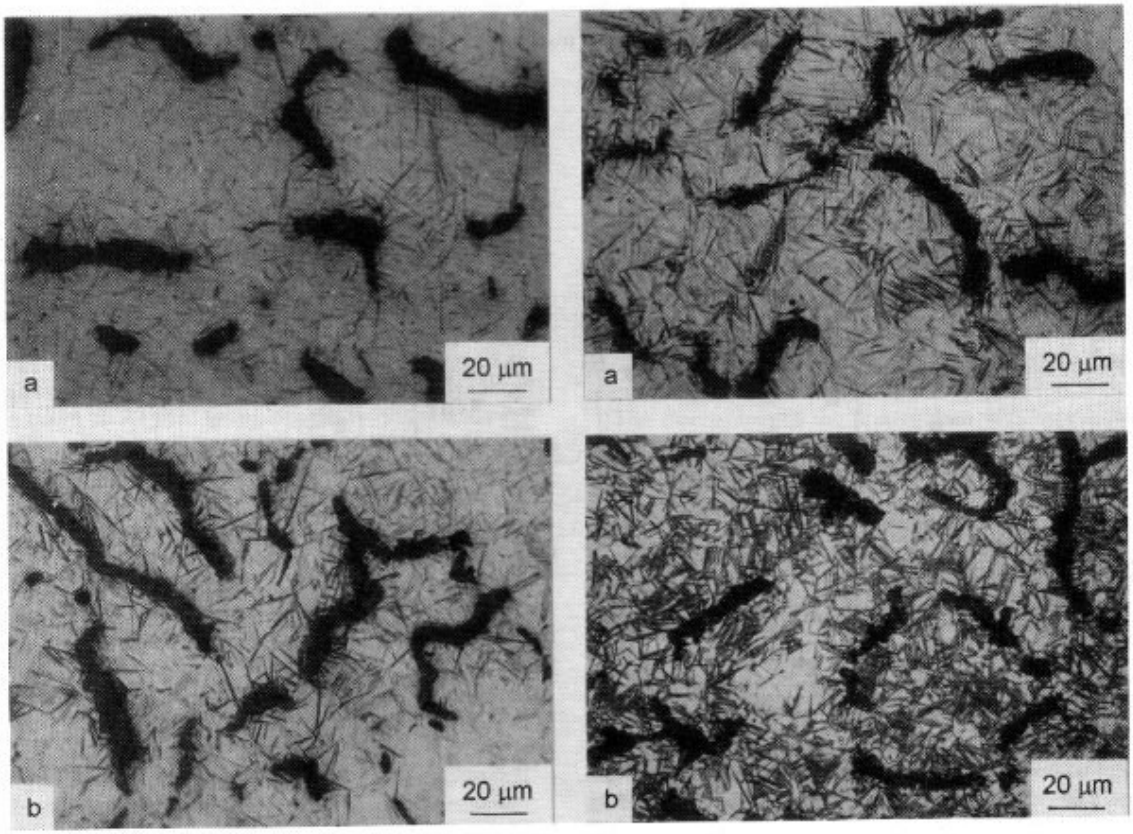

Fig. 5—Microstructure of alloy A on the left and alloy B on the right after (a) 1 min and (b) 2 min of austempering.

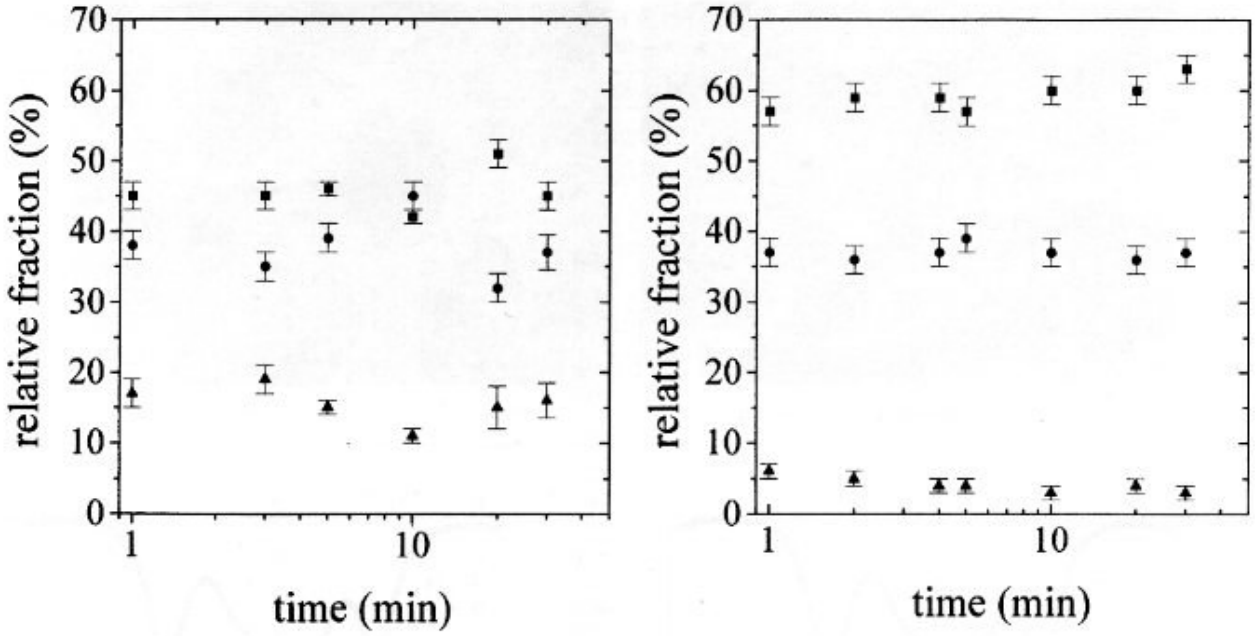

Fig. 6—Evolution of the relative intensities of the magnetic subspectra for different austempering time for alloy A on the left and alloy B on the right: ■ F_1^M, ● F_2^M, and ▲ F_3^M.

ADI (Figure 7). This result indicates that the variation in the constant rate must be ascribed to the morphological differences of the graphite phase.

The morphological differences of graphite particles in cast iron have been studied in previous works,[2,3] which determined that the graphite/matrix interface is 2 to 3 times larger in CG than in nodular graphite. This fact could have an important effect on the nucleation rate of ferrite needles,

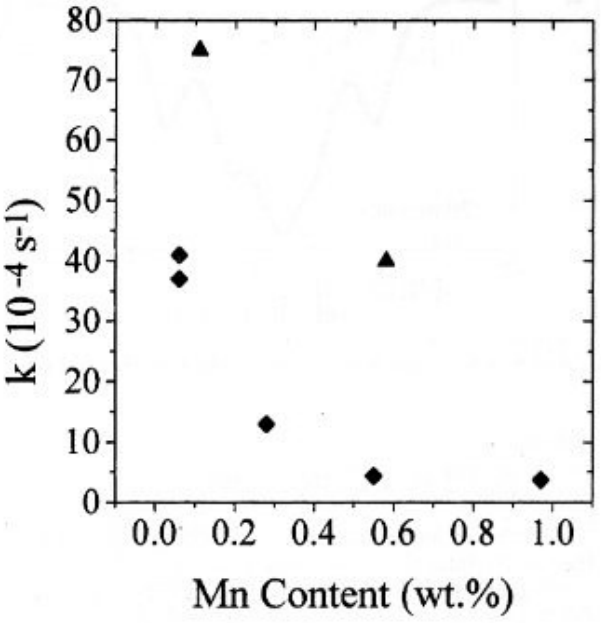

Fig. 7—Constant rate k *vs* Mn content: ◆ ADI, and ▲ austempered CG.

which, as can be seen in Figure 5, occurs at the graphite/austenite interface. The larger interface area in CG cast iron provides more nucleation sites for the ferrite, and, consequently, the kinetics is favored. Figure 8 illustrates ferrite nucleation in CG and nodular cast irons of the same composition (0.22 and 0.24 wt pct of Mn, respectively), austempered with the same thermal cycle after 1 minute of treatment. The nucleation is more noticeable in CG cast iron, revealing a nucleation rate higher than that for ADI.

To follow the evolution of the carbon concentration in austenite, Mössbauer spectra were recorded in the velocity range from −2 to +2 mm/s. Spectra belonging to different steps of the austempering treatment are shown in Figure 9, where the austenite pattern is observed, in detail, to be sitting on the two central lines of the magnetically split ferrite/martensite background. These signals were taken into account using two Lorentzian lines. Austenite spectra were analyzed in the frame of the model proposed by Uwakweh *et al.*,[18] which accounts for the different Fe-C configurations in the fcc lattice, assuming an Fe_8C_{1-y} ($0 < y < 1$) solid solution and a repulsive interaction between carbon atoms. Three different hyperfine interactions were used to reproduce the spectra that were associated with a (1) iron atoms without near-neighbor or next-near-neighbor C atoms (Γ_{00}), (2) iron atoms with only one near-neighbor C atom (Γ_{10}), and (3) iron atoms without near-neighbor C atoms, but with n second-neighbor C atoms (Γ_{0n}). The resulting hyperfine parameters are reported in Table III for each austempering time. The relative fractions of each subspectra (f_{ij}) normalized with respect to the total relative fraction of austenite, are also included. The Γ_{00}-component isomer shift was held fixed along the fits over the whole austempering time interval studied. Its contribution is observed to decrease with increasing time. The Γ_{0n} singlet slightly shifts to positive velocities

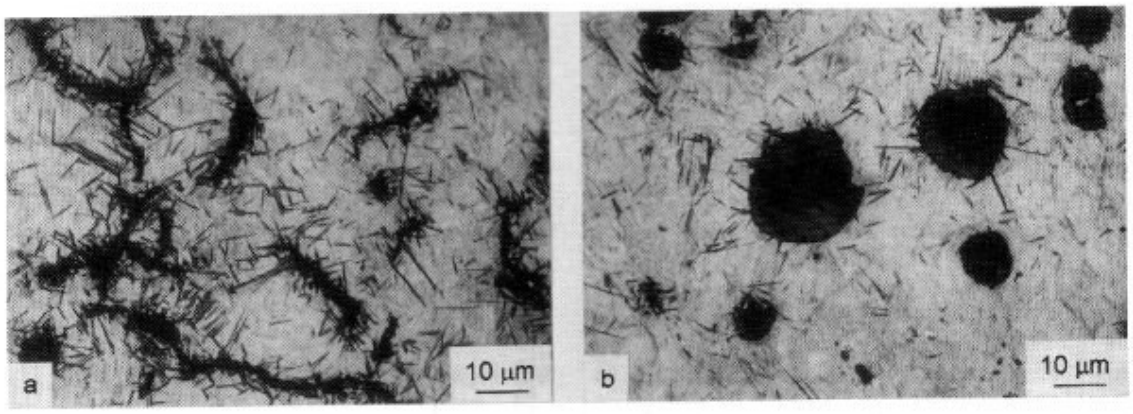

Fig. 8—Ferrite nucleation in (*a*) austempered CG and (*b*) ADI.

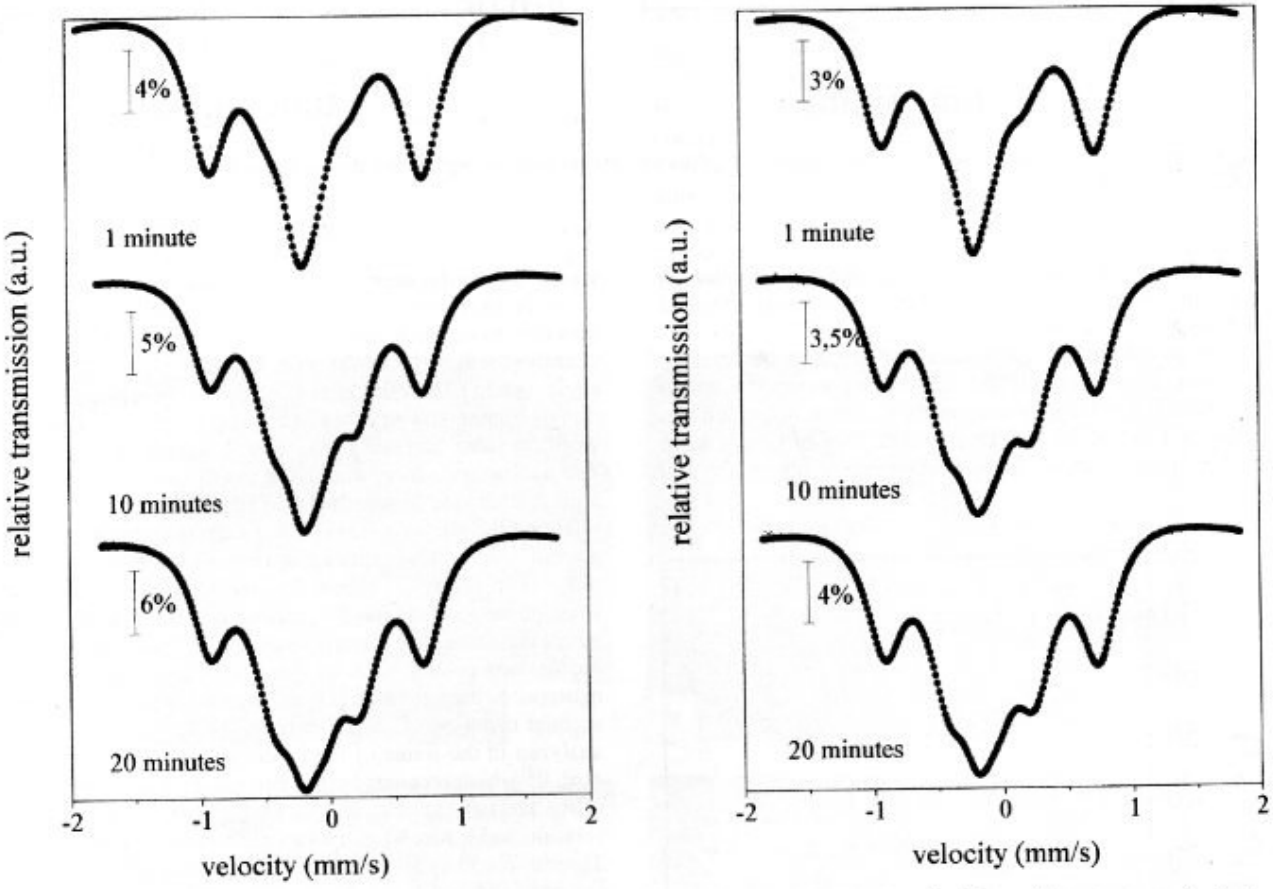

Fig. 9—Mössbauer austenite pattern obtained using a low velocity range for alloy A on the left and alloy B on the right at different austempering times.

as the austempering time increases. Its intensity is practically constant, in agreement with the results of Reference 18. The hyperfine parameters belonging to Γ_{10} are nearly constant, the only observed change being the increase of its intensity.

Assuming the same Mössbauer–Lamb factor for all the sites in austenite, the atomic carbon concentration of this phase can be determined using the occupation probabilities of Reference 18:

$$f_{00} = 3y/4 \quad f_{10} = (6(1 - y))/8 \quad f_{0n} = 0.25$$

An average atomic carbon concentration obtained from the relative intensities associated with Γ_{10} and Γ_{00} was performed, and the results are displayed in Figure 10, where the weight-percent scale is also displayed. An increase of the carbon concentration with the austempering time is observed for both alloys; alloy B displays higher values.

Table III. Hyperfine Parameters and Relative Percentages of the Three Different Carbon Environments Found in Austenite for Both Alloys

Alloy A

Time (min)	Γ_{10} δ_{IS} (mm/s)	Γ_{10} Δ (mm/s)	Γ_{10} $F_{\Gamma 10}$ (Pct)	Γ_{10} f_{10} (Pct)	Γ_{0n} δ_{IS} (mm/s)	Γ_{0n} $F_{\Gamma 0n}$ (Pct)	Γ_{0n} f_{0n} (Pct)	Γ_{00} δ_{IS} (mm/s)	Γ_{00} $F_{\Gamma 00}$ (Pct)	Γ_{00} f_{00} (Pct)	f_γ (Pct)
1	-0.03_1	0.65_1	7_1	39_1	0.04_1	3_1	17_1	-0.1	8_1	44_1	18
2	-0.02_1	0.64_1	9_1	46_1	0.05_1	3_1	17_1	-0.1	7_1	37_1	19
3	0.00_1	0.66_1	10_2	44_2	0.06_1	4_1	18_1	-0.1	9_1	38_1	23
4	0.00_1	0.67_1	11_1	44_1	0.06_1	5_1	21_1	-0.1	8_1	35_1	24
5	0.00_1	0.67_1	11_1	44_1	0.06_1	6_1	23_1	-0.1	9_1	33_1	26
10	0.01_1	0.67_1	14_1	48_1	0.05_1	6_1	22_1	-0.1	9_1	29_1	29
20	0.00_1	0.67_1	17_1	58_1	0.07_1	5_1	19_1	-0.1	7_1	23_1	29
30	0.01_1	0.64_1	17_1	61_2	0.06_1	5_1	19_1	-0.1	6_1	20_1	28

Alloy B

Time (min)	Γ_{10} δ_{IS} (mm/s)	Γ_{10} Δ (mm/s)	Γ_{10} $F_{\Gamma 10}$ (Pct)	Γ_{10} f_{10} (Pct)	Γ_{0n} δ_{IS} (mm/s)	Γ_{0n} $F_{\Gamma 0n}$ (Pct)	Γ_{0n} f_{0n} (Pct)	Γ_{00} δ_{IS} (mm/s)	Γ_{00} $F_{\Gamma 00}$ (Pct)	Γ_{00} f_{00} (Pct)	f_γ (Pct)
1	-0.01_1	0.66_1	9_2	41_2	0.05_1	3_1	16_1	-0.1	9_1	43_1	21
3	0.01_1	0.67_1	11_2	44_2	0.05_1	6_1	23_1	-0.1	8_1	33_1	25
4	0.01_1	0.67_1	14_3	48_3	0.06_1	7_1	23_1	-0.1	8_1	29_1	29
5	0.01_1	0.66_1	16_1	52_1	0.05_1	6_1	21_1	-0.1	8_1	27_1	30
10	0.01_1	0.67_1	15_3	51_3	0.05_1	8_2	25_2	-0.1	7_2	24_2	30
20	0.01_1	0.67_1	16_2	58_2	0.06_1	6_1	21_1	-0.1	5_1	21_1	27

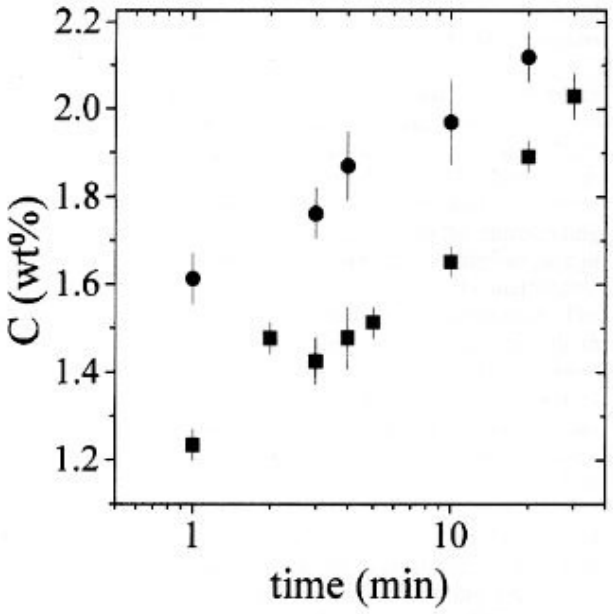

Fig. 10—Austenite carbon concentration as a function of the austempering time: ■ alloy A, and ● alloy B.

The determination of the austenite carbon content permits an analysis of the driving force of the austempering transformation, which has been established[8,9,19] to be proportional to the difference in content $(C_\gamma - C_\gamma^o)$, where C_γ is the maximum carbon content of the austenite stabilized during austempering and C_γ^o is the austenite carbon content in the austenite after austenization. The value of C_γ^o can be calculated using the following empirical relationship[20]

$$C_\gamma^o = -0.435 + 0.335 \times 10^{-3}\, T_\gamma + 1.61 \times 10^{-6}\, T_\gamma^2 + \\ + 0.006\ (\text{wt pct Mn}) - 0.11\ (\text{wt pct Si}) \\ + 0.014\ (\text{wt pct Cu}) \ldots$$

The values obtained for C_γ^o were 0.92 wt pct for alloy A and 0.94 wt pct for alloy B, while the maximum C_γ value can be obtained from the experimental data displayed in Figure 8. The $(C_\gamma - C_\gamma^o)$ values are higher for alloy B than for alloy A, being 1.2 and 1, respectively, suggesting a higher driving force for this alloy with respect to the high-Mn alloy, in concordance with the previously reported k values.

In brief, the present results clearly indicate that the transformation during *stage I* of austempering is strongly influenced by the Mn content. As in the case of ADI, the increment of the Mn content slows down the nucleation and growth rates of ferrite needles. In addition, the graphite morphology influences the austempering kinetics, because graphite particles act as a substrate for ferrite nucleation. Since a CG morphology presents a larger graphite/matrix interface than does a nodular morphology, ferrite nucleation is favored, and, hence, a faster kinetics is observed than in nodular cast iron.

IV. CONCLUSIONS

The kinetics of austempering transformation in CG cast irons with two different Mn concentrations (0.11 and 0.58 wt pct) have been thoroughly examined using Mössbauer spectroscopy, following the evolution of the austenite relative fraction. The results were analyzed with the Johnson–Mehl equation to determine the kinetics parameters n and k. It was found that the constant rate is higher for the low-Mn alloy than for the high-Mn alloy, being $7.47 \times 10^{-3}\ s^{-1}$ and $3.9 \times 10^{-3}\ s^{-1}$, respectively, confirming that Mn slows down the kinetics. This result is corroborated by the analysis of the magnetic subspectra, metallographic observations, and

the driving-force values deduced from the difference ($C_\gamma - C_\gamma^{\alpha}$) obtained through the determination of the austenite carbon concentration.

The effect of graphite morphology on austempering kinetics was also evaluated as a function of the constant rate. The values obtained in austempered CG cast iron were higher than those in ADI, corroborating the faster kinetics in CG cast iron. This fact is coherent with the larger graphite/matrix interface of CG than that of nodular graphite, presenting more nucleation sites for the ferrite needle nucleation, which favors the kinetics.

ACKNOWLEDGMENTS

This work was partially supported by the following Argentine institutions: PID4326, Consejo Nacional de Investigaciones Científicas y Técnicas (CONICET); PICT1277 Agencia Nacional de Promoción Científica y Tecnológica (ANPCyT); Fundación Antorchas; Comisión de Investigaciones Científicas de la Provincia de Buenos Aires (CICPBA) and Laboratorio de Entrenamiento Multidisciplinario para la Investigación Tecnológica (LEMIT-CICPBA).

REFERENCES

1. J.M. Guilemany and N. Llorca: *Metall. Trans. A*, 1990, vol. 21A, pp. 895-99.
2. I. Riposan and Chisamera: *Proc. 3th Int. Conf. on ADI, AFS*, 1991, pp. 437-55.
3. I. Riposan and Chisamera: *Conf. Proc., Cast Iron IV, Materials Research Society*, Pittsburgh, PA, 1990, pp. 195-202.
4. H. Bayati, A.L. Rimmer, and R. Elliott: *Cast Met.*, 1994, vol. 7 (1), pp. 11-24.
5. B.T. Sim and R. Elliott: *Mater. Sci. Technol.*, 1998, vol. 14 (2), pp. 89-96.
6. M. Ron: in *Applications of Mösbauer Spectroscopy*, R.L. Cohen, Academic Press, New York, NY, 1976, vol. II, pp. 329-88.
7. K.B. Rundman and R.C. Klug: *AFS Trans.*, 1982, vol. 90, pp. 499-508.
8. N. Darwish and R. Elliott: *Mater. Sci. Technol.*, 1993, vol. 9 (7), pp. 572-85.
9. T.N. Rouns and K.B. Rundman: *AFS Trans.*, 1987, vol. 95, pp. 851-74.
10. F.E. Fujita: in *Topics in Applied Physics: Mössbauer Spectroscopy*, V. Gonser, ed., Springer-Verlag, Berlin, 1975, pp. 201-36.
11. F.E. Fujita and S. Nasu: *Mater. Sci. Forum*, 1989, vol. 37, pp. 235-44.
12. R.D. Doherty: in *Physical Metallurgy*, R.W. Cahn and P. Haansen, eds., North-Holland, 1996, vol. 2, pp. 1363-1505.
13. Y.C. Liu, J.M. Schissler, and A. Munteanu: *La Rev. Mét.*, 1994, vol. 91, (5) pp. 815-26.
14. D.G. Rancourt, A.M. Mc Donald, A.E. Lalonde, and J.Y. Ping: *Am. Mineralogist*, 1993, vol. 78, pp. 1-7.
15. T.W. Christian: *The Theory of Transformation in Metals and Alloys*, Pergamon Press, Oxford, United Kingdom, 1965, pp. 525-48.
16. S.F. Hubert: *J. Br. Cer. Soc.*, 1969, p. 11 (as quoted in Ref. 13).
17. B.V. Kovacs: *Proc. 3th Int. Conf. on ADI, AFS*, 1991, vol. I, pp. 241-70.
18. O.N.C. Uwakweh, J.P. Bauer, and J.M. Génin: *Metall. Trans. A*, 1990, vol. 21A, pp. 589-602.
19. N. Darwish and R. Elliott: *Mater. Sci. Technol.*, 1993, vol. 9 (7), pp. 586-602.
20. F. Neumann: in *Research in Cast Iron*, H.D. Merchant, ed., Gordon and Breach, Reading, MA, 1965, p. 659 (as quoted in Ref. 5).